Wavelength-accurate nonlinear conversion through wavenumber selectivity in photonic crystal resonators

Jordan R. Stone,[1,2,*] Xiyuan Lu,[1,2] Gregory Moille,[1,2] Daron Westly,[2] Tahmid Rahman,[1,2] and Kartik Srinivasan[1,2,†]

[1] *Joint Quantum Institute, NIST/University of Maryland, College Park, MD 20742*

[2] *National Institute for Standards and Technology, Gaithersburg, MD 20899*

(Dated: November 28, 2023)

Abstract

Integrated nonlinear wavelength converters transfer optical energy from lasers or quantum emitters to other useful colors, but chromatic dispersion limits the range of achievable wavelength shifts. Moreover, because of geometric dispersion, fabrication tolerances reduce the accuracy with which devices produce specific target wavelengths. Here, we report nonlinear wavelength converters whose operation is not contingent on dispersion engineering; yet, output wavelengths are controlled with high accuracy. In our scheme, coupling between counter-propagating waves in a photonic crystal microresonator induces a photonic bandgap that isolates (in dispersion space) specific wavenumbers for nonlinear gain. We demonstrate the wide applicability of this strategy by simulating its use in third harmonic generation, Kerr-microcomb dispersive wave formation, and four-wave mixing Bragg scattering. In experiments, we demonstrate Kerr optical parametric oscillators in which such wavenumber-selective coupling designates the signal mode. As a result, differences between the targeted and realized signal wavelengths are < 0.3 percent. Moreover, leveraging the bandgap-protected wavenumber selectivity, we continuously tune the output frequencies by nearly 300 GHz without compromising efficiency. Our results will bring about a paradigm shift in how microresonators are designed for nonlinear optics, and they make headway on the larger problem of building wavelength-accurate light sources using integrated photonics.

* jstone12@umd.edu

† kartik.srinivasan@nist.gov

I. INTRODUCTION

Controlling integrated microsystems to generate light with properties specifically geared to applications is a fundamental ambition of photonics research. For example, optical atomic clocks require ultra-coherent laser light with wavelengths precisely matched to atomic transitions, and future hybrid quantum networks will interface sources of nonclassical light (e.g., single photons) tuned to qubit wavelengths [1–4]. A powerful tool to meet the demands of such systems is optical nonlinearity, which can mold light on a quantum level and stimulate wavelength conversion (e.g., by four-wave mixing (FWM)) for spectral access beyond conventional laser gain. In particular, optical microresonators with Kerr ($\chi^{(3)}$) nonlinearity have, after multiple groundbreaking demonstrations, become a linchpin of nonlinear photonics. They support microcombs for frequency synthesis, timekeeping, and sensing [5–8]; optical parametric oscillators (μOPOs) for wavelength-flexible sources of laser light [9–11], squeezed light [12, 13] and (when operated below threshold) entangled photon pairs [14, 15]; four-wave mixing Bragg scattering (FWM-BS) for spectral translation of single photons [16]; third harmonic generation (THG) [17, 18]; and more. Although appreciable efficiencies have been shown in some cases, it remains a challenge to ensure *a priori* (i.e., before testing) that a specific device will achieve the desired combination of wavelength accuracy and efficiency.

To elucidate the problem, we recall some basic design considerations for Kerr-nonlinear microresonators, focusing on commonly used microring devices. Fundamentally, energy and momentum conservation regulate FWM [19]; therefore, to within (approximately) a resonator linewidth, a set of resonator modes should obey:

$$\sum_i \nu_i = \sum_j \nu_j, \tag{1a}$$

$$\sum_i m_i = \sum_j m_j, \tag{1b}$$

where m_i is the azimuthal number (fundamentally related to the wavenumber) associated with a resonator mode with frequency ν_i, and left-hand (right-hand) terms denote photons created (annihilated) in the FWM process. Equation 1 is exact when ν_i and m_i refer to field quantities. In general, group velocity dispersion (GVD) induces a frequency mismatch, such that a set of modes satisfying Eq. 1b does not simultaneously satisfy Eq. 1a. The strategic

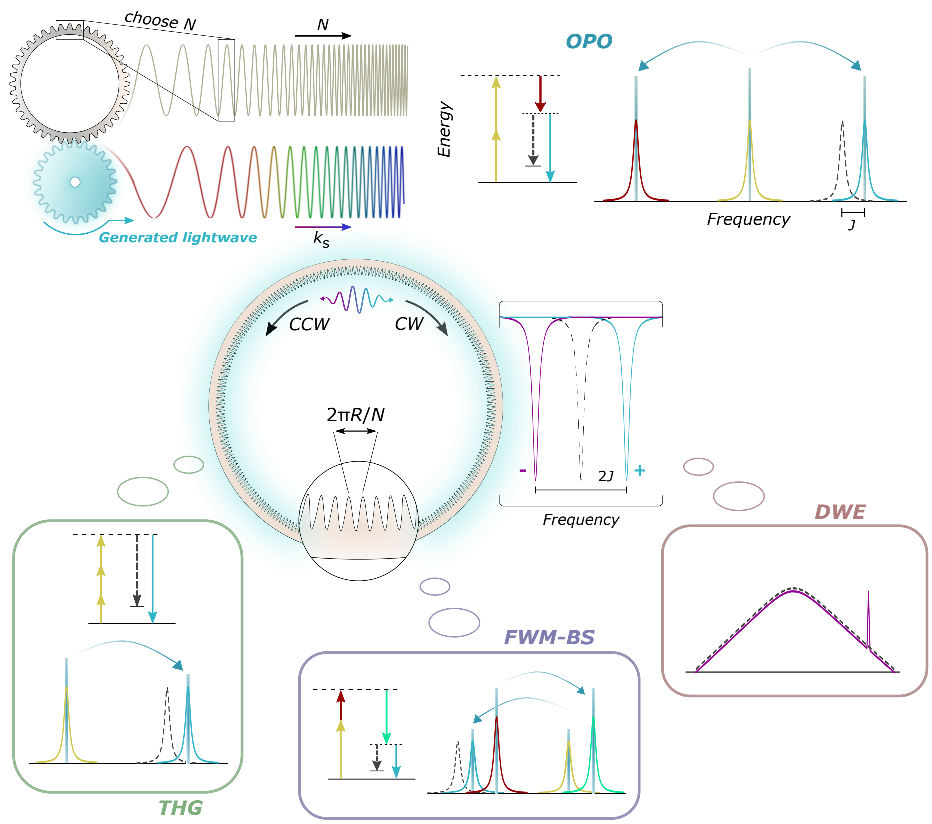

FIG. 1. **Conceptual depictions of wavenumber-selective nonlinear wavelength conversion in Kerr photonic crystal microresonators.** Spatial modulation of the microresonator inner sidewall (pictured center) with a grating period $2\pi R/N$, where N is an integer, coherently couples clockwise (CW) and counter-clockwise (CCW) travelling-wave modes with the azimuthal mode number $m_{\rm s} = N/2$. Wavenumber-selective coherent coupling induces a frequency splitting between two supermodes, denoted '$+'$ and '$-'$, with frequency separation $2J$, where J is proportional to the sidewall modulation amplitude. We link the spatial frequency of sidewall modulation, N, to the wavenumber, $k_{\rm s} = N/2R$, of an output wave that is generated via nonlinear wavelength conversion. Hence, the photonic crystal resonator functions as a sort of gear, as illustrated in the upper left, to accurately control the wavelengths produced by a given device. Bottom portion: In resonators with normal group velocity dispersion (GVD), four-wave mixing (FWM) cannot occur between travelling-wave modes due to energy non-conservation (see energy level diagrams), but frequency matching can be realized using one of the supermodes. This allows, for example, optical parametric oscillation (OPO), third harmonic generation (THG), and FWM Bragg scattering (FWM-BS) in microresonators with purely normal GVD, and dispersive-wave enhancements (DWEs) in microresonators with purely anomalous GVD that support soliton microcombs.

‘dispersion engineering’ of modes to satisfy both parts of Eq. 1 is ubiquitous in guided-wave nonlinear photonics, with the most popular approach being to complement material dispersion with dispersion arising from the microresonator geometry [20–22]. However, modeling broadband spectra, such as octave-spanning microcombs or μOPOs with widely-separated wavelengths, often requires retaining six or more orders in a Taylor expansion of $\nu_{\mathrm{i}}(m_{\mathrm{i}})$ around the pump wavelength [23, 24]. In this regime, the mode wavelengths that satisfy Eq. 1 are extremely sensitive to geometry. Hence, small errors in the device geometry (arising from either fabrication uncertainties or incomplete modeling) can amount to significant differences between the simulated and experimentally-observed spectrum. This necessitates the fabrication of many (often, hundreds or more) devices with nanometer-scale parameter variations. Ultimately, one negotiates a trade-off between the number of devices that require testing and the dispersion tolerance of a given application. In many cases, a simple geometry-based solution to realize a particular GVD (e.g., one based on controlling the dimensions of a waveguide) does not exist. To make matters worse, unwanted nonlinear couplings (e.g., Raman scattering, mode competition, etc.) can compete with or even suppress the targeted process [16, 25–27].

Here, we demonstrate Kerr-nonlinear wavelength conversion for which the m values of participating resonator modes are guaranteed from design; yet, our method actually alleviates design constraints, naturally suppresses unwanted nonlinear couplings, and does not rely on sensitive control of higher-order GVD. We show how wavenumber-selective coherent coupling (hereafter referred to simply as ”coherent coupling”) between counter-propagating waves in a photonic crystal microresonator induces controlled frequency splittings that balance the underlying GVD to satisfy Eq. 1. We analyze μOPO, THG, dispersive-wave enhancement (DWE) in microcombs, and FWM-BS by introducing coherent coupling into simulations of those systems, and we prove our ideas experimentally using the flexible example of μOPO. Through the photonic crystal grating period, we dictate m values for the signal modes in three different μOPOs, and we showcase their tolerance to higher-order GVD by reproducing the same signal wavelength when pumping four separate modes of a single device. Generated signal wavelengths agree with simulations to within 0.3 %. We characterize the μOPOs by their threshold power and conversion efficiency, and we find that our measurements agree with a model based on the Lugiato-Lefever Equation. Finally, we highlight the protected nature of our method by tuning the μOPO output frequencies continuously over 300 GHz without sacrificing efficiency or inducing mode hopping. Our work re-envisions the design process for nonlinear wavelength converters, enables nonlinear optics in new spectral regions and with strongly-dispersive materials, and invites fundamental studies of nonlinear physics in photonic crystal microresonators.

II. PHOTONIC CRYSTAL-MEDIATED FWM

Figure 1 depicts a photonic crystal microresonator and illustrates the four FWM processes we study. For concreteness, we consider silicon nitride (SiN) microrings where the ring width, RW', varies along the inner boundary according to $RW' = RW + A_{\mathrm{mod}}\cos(N\theta)$, where RW is the nominal ring width, N is an integer, and θ is the resonator azimuthal angle. Therefore, the spatial period of modulation is $2\pi R/N$, where R is the ring radius. The modulation creates a refractive index grating that coherently couples clockwise (CW) and counter-clockwise (CCW) travelling-wave (TW) modes with the azimuthal number $m = N/2$, where m is an integer related to the wavenumber, k, by $k = m/R$. Hence, we say the coherent coupling is "wavenumber-selective." The coupling rate, J, is proportional to A_{mod} and corresponds to half the frequency splitting between two supermodes, denoted '+' and '-' for the higher- and lower-frequency resonances, respectively (pictured center). This type of resonator has numerous functionalities, including for sensing [28, 29] and the slowing of light [30]. In the context of nonlinear optics, pump mode hybridization has been used to induce spontaneous pulse formation and facilitate parametric oscillations in resonators with normal GVD. [31–33]. Moreover, modulations with different N values can be combined to realize multi-wavelength dispersion engineering [34–36]. In these experiments and others, J could be made larger than the resonator free spectral range (FSR) without reducing the quality factor (Q).

In our experiments, we focus on μOPOs, which generate monochromatic signal and idler waves from a continuous-wave (CW) pump laser through resonantly-enhanced degenerate FWM, as shown at the top (energy diagram and optical spectrum) of Fig. 1. Momentum conservation requires $2m_{\mathrm{p}} = m_{\mathrm{s}} + m_{\mathrm{i}}$, where m_{p}, m_{s}, and m_{i} are azimuthal numbers for the pump, signal, and idler modes, respectively. Hence, mode pairs with $m = m_{\mathrm{p}} \pm \mu$, where μ is an integer, may support μOPO if their resonance frequencies obey Eq. 1a. In general, GVD prevents such frequency matching; *i.e.*, the associated FWM process does not conserve energy. In Fig. 1, gray dashed lines in the energy diagrams and optical spectra illustrate how GVD suppresses FWM. To quantify this concept, we define the frequency mismatch as:

$$\Delta\nu = \nu_{\mu} + \nu_{-\mu} - 2\nu_0, \tag{2}$$

where ν_0 is the pump mode frequency, and ν_{μ} is the mode frequency associated with the azimuthal number $m_{\mathrm{p}} + \mu$. Normal GVD gives $\Delta\nu < 0$ for all μ and thus prevents FWM. Nonetheless, applying an appropriate shift to ν_{μ} (or $\nu_{-\mu}$) will restore energy conservation and activate the μOPO, as illustrated by the blue lines in Fig. 1. We can realize this shift via the '+' supermode; changing to the '+' basis gives the transformation:

$$\Delta\nu_{+} = \begin{cases} \Delta\nu_{\mathrm{CW}} + J, & m = \{N/2, 2m_{\mathrm{p}} - N/2\} \\ \Delta\nu_{\mathrm{CW}}, & \text{else} \end{cases} \tag{3}$$

where $\Delta\nu_{\mathrm{CW}}$ is the frequency mismatch in the CW basis. Hence, we select m_{s} by choosing $N = 2m_{\mathrm{s}}$, and the μOPO is activated when $J = -\Delta\nu_{\mathrm{CW}}$. Note that, from Eq. 2, $\Delta\nu_{+}(\mu) = \Delta\nu_{+}(-\mu)$; hence, the mismatch is shifted for both signal and idler modes. In the Supplemental Fig. 2, we theoretically compare this approach to the case where $N = 2m_{\mathrm{p}}$ [32, 33], and we identify a number of key differences; namely, choosing $N = 2m_{\mathrm{s}}$ improves robustness, wavelength accuracy, and tunability of the μOPO.

Importantly, coherent coupling in photonic crystal resonators can facilitate other FWM processes besides μOPO, as illustrated in Fig. 1. Specifically, we explore THG, FWM-BS, and DWE, all of which involve wide spectral gaps between their constituent wavelengths and thus exhibit $\Delta\nu$ spectra that are difficult to control exclusively via the microresonator cross-sectional geometry. In each case, we can re-define $\Delta\nu$ according to Eq. 1a (see Supplemental Sec. I) and employ coherent coupling to restore energy conservation by balancing $\Delta\nu_{\mathrm{CW}}$ with J. In Fig. 1, energy diagrams and optical spectra show how shifting the frequency of one mode can promote THG and FWM-BS. The DWE process merits special elaboration. Bright soliton microcombs operate in a regime of anomalous GVD, but certain wavelengths with normal GVD can exhibit local power enhancements (i.e., DWE) [24, 37]. The DWE phenomenon is useful to aid self-referencing, but the dispersive-wave (DW) wavelengths are difficult to control due to their reliance on higher-order GVD. We envision using wavenumber-selective coherent coupling to dictate the m values of DWs. Because of the underlying anomalous GVD, DWs would be resonant with the '-' supermode.

This scheme could operate without tailoring higher-order GVD and deterministically select harmonic wavelengths for self-referencing, thus augmenting microcombs spectrally-tailored with Fourier synthesis [35].

To prove our ideas, we analyze THG, FWM-BS, and DWE in resonators with either purely normal (for THG and FWM-BS) or purely anomalous (for DWE) GVD by including coherent coupling in simulations of those systems. We reserve μOPO simulations for the next section, where we aim to verify our model with experiments. We use a set of coupled-mode equations (CMEs) to simulate THG, and a pair of coupled Lugiato-Lefever Equations (LLEs) to simulate FWM-BS and DWE (for details, see Supplemental Sec. I). Importantly, we include the coherent coupling explicitly in our models; i.e., we do not manually insert frequency shifts into the GVD, since this would not account for the hybridization of CW/CCW modes. We define the mode spectra and perform simulations in the CW/CCW basis. To include coherent coupling, we allow one CW mode to exchange energy with its CCW counterpart at a coupling rate J that is continuously tunable. In Fig. 2, we present simulated optical spectra for THG, FWM-BS, and DWE. The gray data correspond to simulations with $J = 0$, while blue or purple data (when utilizing the '+' or '-' supermodes, respectively) correspond to simulations where J is tuned to maximize the signal (or DW) power.

In our simulations, we assign to all modes a (critically-coupled) loaded linewidth $\kappa/2\pi =$ 500 MHz. In THG simulations, we set $\Delta\nu_{\mathrm{CW}} = 12.5$ GHz and $P_{\mathrm{in}} = 250$ μW, where P_{in} is the pump power. This P_{in} value efficiently drives THG but is below the saturation power (see Supplemental Fig. 1). We apply coherent coupling to the third-harmonic mode. When $J = 0$, the third harmonic power, $P_{3H} \approx 2.7$ nW. We find that $J = 12.425$ GHz maximizes P_{3H}, in accordance with Eq. 3, increasing it to $P_{3H} \approx 3$ μW, as shown in Fig. 2a.

To model FWM-BS, we simulate a microresonator pumped by two separate pump lasers resonant with modes $m = 370$ and $m = 420$. $P_{\mathrm{in}} = 5$ mW for both pump lasers. A low-power input seed, resonant with mode $m = 410$, is also injected into the resonator. FWM-BS converts input seed photons to output signal photons resonant with $m = 360$. We set $D_2/2\pi = -25$ MHz/mode, where D_2 is the second-order term in a Taylor series expression of the integrated dispersion, $D_{\mathrm{int}} = \nu_\mu + (\nu_0 - \mu\mathrm{FSR})$. This D_2 value corresponds to $\Delta\nu_{\mathrm{CW}} = 12.5$ GHz. We apply coherent coupling to the signal mode. When $J = 0$, virtually no seed photons are converted. When $J = 12.6$ GHz, ≈ 25 % of input photons

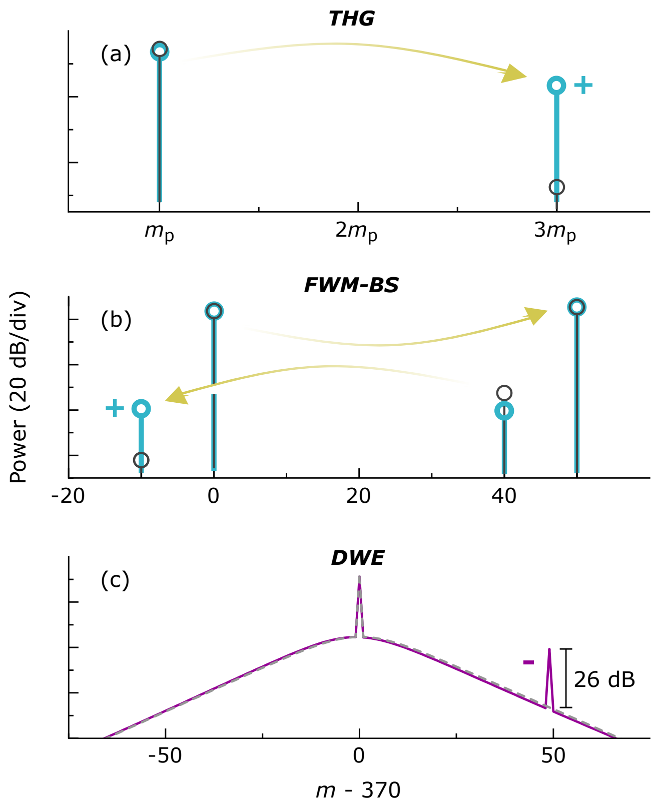

FIG. 2. **Simulations of nonlinear wavelength conversion in Kerr photonic crystal microresonators.** The m values designated for coherent coupling are marked by a blue '+' or a purple '-', depending on which supermode is utilized. (a) Simulated THG spectrum, both with (blue) and without (gray) photonic crystal-mediated coherent coupling (J). The simulation parameters are $\Delta\nu_{\mathrm{CW}} = 12.5$ GHz, $J = 12.425$ GHz (blue data only), and $P_{\mathrm{in}} = 250$ μW. (b) Simulated FWM-BS spectrum, both with (blue) and without (gray) coherent coupling. The simulation parameters are $D_2/2\pi = -25$ MHz/mode, which corresponds to $\Delta\nu_{\mathrm{CW}} = 12.5$ GHz, $J = 12.6$ GHz (blue data only), and $P_{\mathrm{in}} = 5$ mW for both pump lasers. (c) Simulated Kerr microcomb spectrum with (purple) and without (dashed gray) coherent coupling. Coherent coupling is used for dispersive wave enhancement (DWE), to increase the power of a single microcomb tone by 26 dB. The simulation parameters are $D_2/2\pi = 10$ MHz/mode, $J = 13.75$ GHz (purple data only), and $P_{\mathrm{in}} = 15$ mW. Higher-order nonlinear effects such as Raman scattering and self-steepening are neglected. Definitions of $\Delta\nu$ for THG and FWM-BS are given in Supplemental Material.

are converted to wavelength-shifted output photons, as shown in Fig. 2b. Notably, Liu *et al.* recently proposed a dispersion engineering approach to FWM-BS that is also based on coherent coupling between CW/CCW modes [38].

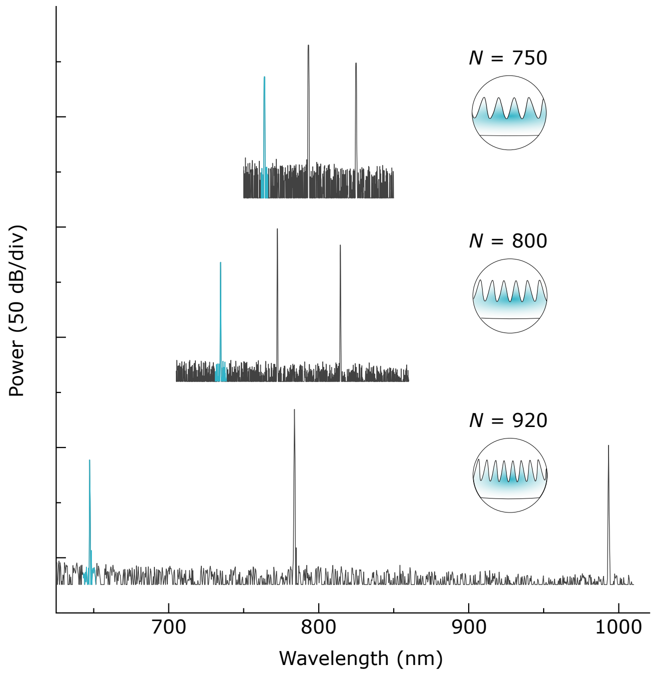

FIG. 3. **Wavenumber-selective μOPO in Kerr photonic crystal microresonators.** Optical spectra generated in three μOPO devices. From top to bottom, $N = (750, 800, 920)$, and $A_{\mathrm{mod}} = (5, 10, 25)$ nm. In each spectrum, the line corresponding to the signal wave is colored blue, and the signal mode number, $m_{\mathrm{s}} = N/2$. Every device exhibits normal GVD at the pump, signal, and idler wavelengths.

To simulate DWE, we set $D_2/2\pi = 10$ MHz/mode and apply coherent coupling to the $m = 419$ mode. A laser, resonant with mode $m = 370$, pumps the resonator with $P_{\mathrm{in}} = 15$ mW. When $J = 0$, the microcomb spectrum exhibits a smooth sech^2 profile with no DWEs. When $J = 13.75$ GHz, we observe a 26 dB power enhancement at the targeted mode, as shown in Fig. 2c. In Supplemental Sec. I, we characterize our simulations in more detail. Remarkably, our modeling captures wavelength conversion into the supermodes, thus illustrating the applicability of our scheme to a variety of Kerr-nonlinear processes.

To validate the main elements of our approach in experiments, we choose an additional Kerr-nonlinear process, that of degenerately-pumped μOPO. In processes like THG and FWM-BS, the potential output wavelength is known *a priori* from the input wavelengths,

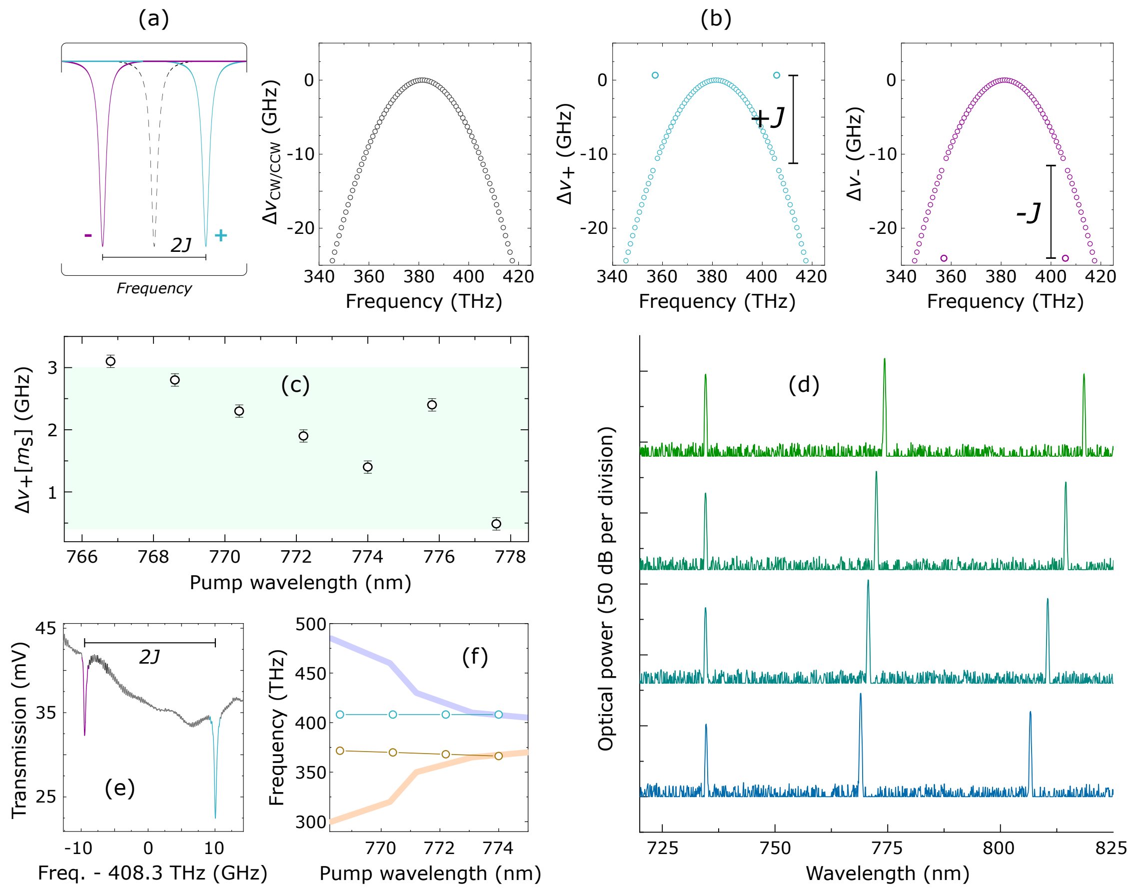

FIG. 4. **Optical parametric oscillation using selective splitting in undulated microresonators (OPOSSUM).** (a) Conceptual transmission spectrum illustrating the frequency splitting of a travelling-wave mode (gray dashed line) into two standing-wave supermodes with frequency separation $2J$. (b) Simulated $\Delta\nu$ spectra of an OPOSSUM device in the CW/CCW basis (left), the '+' basis (center), and the '-' basis (right). In the '+' basis, a single mode pair is frequency matched to allow FWM, and normal GVD mismatches all other mode pairs. (c) $\Delta\nu_+$ versus pump wavelength for an OPOSSUM device with $R = 25$ μm, $RW = 925$ nm, $H = 600$ nm, and $N = 800$. Vertical error bars correspond to the range in $\Delta\nu_+$ values obtained when the measurement is repeated many (≈ 10) times. The pale green stripe indicates $\Delta\nu_+$ values conducive to μOPO. (d) Optical spectra obtained from pumping four different modes (with wavelengths between 768 nm to 774 nm) in the OPOSSUM device. (e) Transmission spectrum of the same device showing '+' and '-' supermodes (blue and purple, respectively) with frequency separation $2J \approx 20$ GHz. (f) OPOSSUM signal (blue circles) and idler (gold circles) frequencies versus pump wavelength. The pale stripes show the same data, taken from Ref. [9], for a device without coherent coupling that relies on higher-order GVD engineering for frequency matching.

with the efficiency of conversion depending on $\Delta\nu$ (as well as other parameters not dependent on the phase- and frequency-matching strategy, namely, resonator-waveguide coupling [16]). In contrast, the μOPO output wavelengths are not determined solely by the input wavelengths, but can widely vary depending on GVD. Therefore, μOPOs provide an ideal experimental test of wavenumber-selective FWM.

To this end, we perform experiments that demonstrate *a priori* control over m_s in μOPO devices with $N = 2m_\mathrm{s}$. In Fig. 3, we present optical spectra generated in three different photonic crystal microresonators with RW' modulations parameterized by $N = (750, 800, 920)$ and $A_\mathrm{mod} = (5, 10, 25)$ nm. In each device, A_mod is chosen to balance the underlying normal GVD (in section III, we explain our design process in more detail). We pump a fundamental transverse-electric (TE0) resonator mode near 780 nm, and we observe one of two outcomes: a μOPO with $m_\mathrm{s} = N/2$ when J compensates for $\Delta\nu_\mathrm{CW}$ (i.e., the three spectra in Fig. 3), or a CW state (i.e., no wavelength conversion; data not shown in Fig. 3) preserved by normal GVD and an incommensurate balance of $\Delta\nu_\mathrm{CW}$ and J. We confirm the m_s values from mode transmission spectroscopy, and we measure (simulate) signal wavelengths of 763.5 nm (761.5 nm), 735 nm (735.8 nm), and 648 nm (649.9 nm). This binary distribution of measurement outcomes affirms the protected nature of wavelength conversion in our experiments.

III. OPOSSUM

We now explain our procedures for designing photonic crystal microresonators and testing them post-fabrication (for details about the fabrication process, see Methods). We refer to the μOPO mechanism as OPOSSUM, which stands for optical parametric oscillation using selective splitting in undulated microresonators. To start, we reiterate the impact of wavenumber-selective coherent coupling on the resonator mode spectrum: CW and CCW modes with $m = N/2$ hybridize into two supermodes with frequency separation $2J$, as illustrated in Fig. 4a. Hence, OPOSSUM devices exhibit three $\Delta\nu$ spectra, denoted $\Delta\nu_\mathrm{CW/CCW}$, $\Delta\nu_+$, and $\Delta\nu_-$, depending on the basis used. To choose values for RW, N, and A_mod (the SiN thickness, H, is fixed by our current stock of SiN, and $R = 25$ μm), we simulate mode spectra using the finite-element method for devices without RW' modulation. We calculate $\Delta\nu_\mathrm{CW}$ according to Eq. 2 and choose a RW value that exhibits broadband normal GVD. Then, we identify a target signal wavelength (e.g., 760 nm, 735 nm, and 650 nm for the

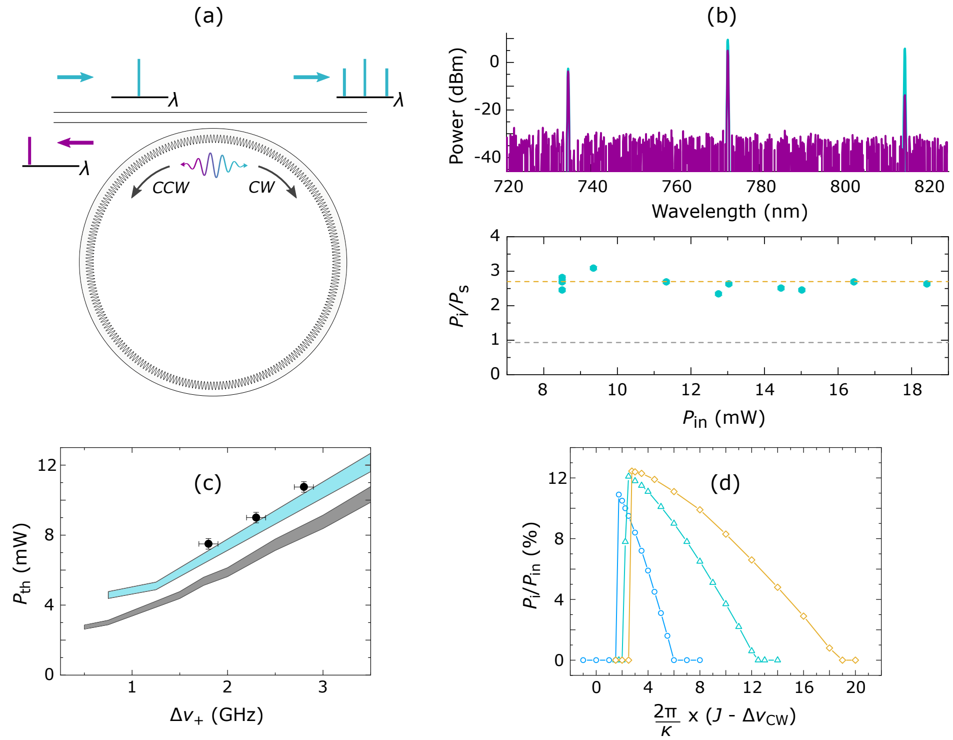

FIG. 5. **Modeling OPOSSUM with the Lugiato-Lefever Equation (LLE).** (a) Illustration of input and output spectra from an OPOSSUM device. Due to coherent coupling between CW and CCW waves in the signal mode, a fraction of signal photons are outcoupled in a direction that is counter-propagating to the injected pump. (b) Top panel: A sample OPOSSUM spectrum calibrated to indicate the on-chip power. Blue data correspond to transmitted light (i.e., light that is outcoupled in a direction co-propagating with the pump laser), and purple data correspond to reflected light. Bottom panel: Measured ratio ($P_{\mathrm{i}}/P_{\mathrm{s}}$) of transmitted idler power (P_{i}) to transmitted signal power (P_{s}) versus P_{in}. The orange (gray) dashed line is a theoretical prediction based on LLE simulations that include (do not include) coherent coupling. (c) Measured threshold power, P_{th}, versus $\Delta\nu_+$. Vertical error bars are due to uncertainties in optical losses between the input and output fibers, calculated as one standard deviation in loss measurements performed for many separate devices. Horizontal error bars correspond to the range in $\Delta\nu_+$ values obtained when the measurement is repeated many (≈ 10) times. The blue and gray stripes are theoretical predictions based on LLE simulations, with (blue) and without (gray) coherent coupling; i.e., the gray stripe is derived from an LLE where $\Delta\nu_{\mathrm{CW}}$ is adjusted to realize frequency matching. The finite thicknesses of theory curves correspond to uncertainties in the value of the Kerr nonlinear coefficient. (d) Simulated idler conversion efficiency, $P_{\mathrm{i}}/P_{\mathrm{in}}$, versus normalized J for $P_{\mathrm{in}} = 10$ mW (blue circles), $P_{\mathrm{in}} = 20$ mW (green triangles), and $P_{\mathrm{in}} = 30$ mW (gold diamonds).

three devices related to Fig. 2b) and choose N accordingly. To select A_{mod}, we fabricate a set of devices with variations in RW, A_{mod}, and N, and we measure the frequency splittings to calibrate $J(N, RW, A_{\mathrm{mod}})$. Using our calibrations, we set A_{mod} for a particular device to balance $\Delta\nu_{\mathrm{CW}}$. Figure 4b depicts simulated $\Delta\nu_{\mathrm{CW/CCW}}$, $\Delta\nu_+$, and $\Delta\nu_-$ spectra for a device with $RW = 925$ nm, $H = 600$ nm, and $N = 800$. Notably, the $\Delta\nu_+$ spectrum is discontinuous at the signal and idler frequencies, where $\Delta\nu_+ = \Delta\nu_{\mathrm{CW}} + J$ (note that, even though coherent coupling is only applied to the signal mode, the $\Delta\nu_+$ values are shifted equally for signal and idler modes because, per Eq. 2, $\Delta\nu_+(\mu) = \Delta\nu_+(-\mu)$). This suggests that OPOSSUM suppresses FWM involving modes other than the targeted signal and idler, since at these frequencies the resonator exhibits strong normal dispersion.

Next, we perform experiments to characterize OPOSSUM. We fabricate the OPOSSUM device simulated in Fig. 4b and measure the TE0 mode wavelengths to calculate $\Delta\nu_+[m_{\mathrm{s}}]$ (i.e., the value of $\Delta\nu_+$ at the targeted signal mode). Importantly, $\Delta\nu_+[m_{\mathrm{s}}]$ depends on m_{p}; hence, tuning the pump wavelength can correct for fabrication uncertainties and, more generally, ensure reliable operation. To concretize this idea, we measure $\Delta\nu_+[m_{\mathrm{s}}]$ versus pump wavelength, as shown in Fig. 4c. We find that $\Delta\nu_+[m_{\mathrm{s}}]$ decreases with increasing pump wavelength, with an exception near 776 nm, where we observe mode crossings at the pump and idler wavelengths. In principle, we can generate a μOPO using any pump mode such that $\Delta\nu_+[m_{\mathrm{s}}] > 0$, provided P_{in} is large enough to induce compensating nonlinear mode-frequency shifts [25]. Realistically, however, we prefer $\Delta\nu_+[m_{rms}] < 3$ GHz. Greater $\Delta\nu_+$ values require $P_{\mathrm{in}} > 50$ mW to produce appreciable signal and idler powers; at this level, absorption-induced temperature shifts can destabilize the μOPO. At the same time, we require $\Delta\nu_+[m_{\mathrm{s}}] > \kappa/4\pi$. In our OPOSSUM devices, we measure typical loaded quality factors between $(5-7)\times 10^5$ (with some dependence on wavelength), so the four pump modes spanning wavelengths 768 nm to 774 nm satisfy these requirements, as indicated by the pale stripe in Fig. 4c. Indeed, pumping any of these modes results in a μOPO. We record the optical spectra and present them in Fig. 4d. As expected, m_{s} is fixed - its value is protected by the wavenumber-selective coherent coupling, with an example transmission spectrum shown in Fig. 4e. In Fig. 4f, we present measurements of the signal and idler frequencies, ν_{s} and ν_{i}, respectively, versus pump wavelength. We overlay similar data (pale stripes), taken from Ref. [9], for a μOPO system that relies on higher-order GVD, where the dispersion sensitivity is apparent from the large shifts in ν_{s} (and ν_{i}) when tuning the pump laser between adjacent pump modes (i.e., with consecutive m_p values). By comparison, OPOSSUM is a robust mechanism for targeting specific wavelengths. In the Supplemental Sec. II, we analyze the microresonator GVD and its connection to such robustness.

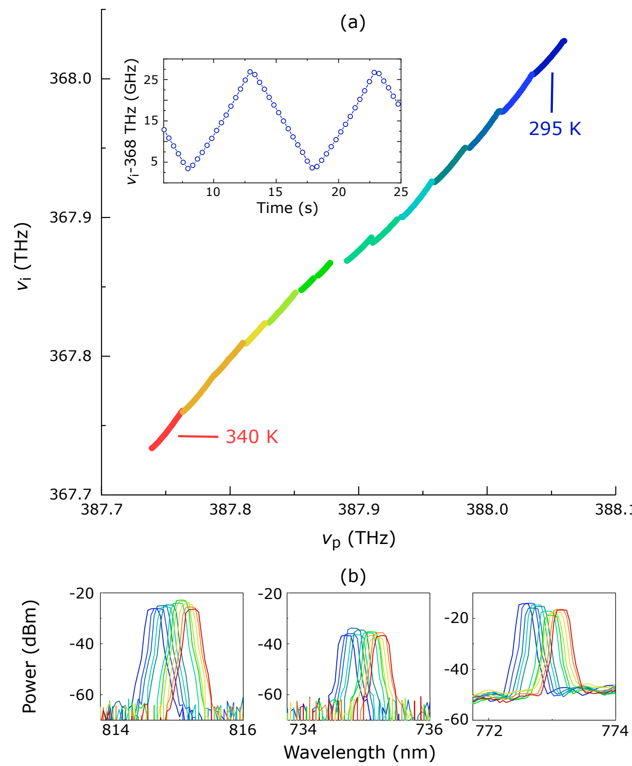

FIG. 6. **Exploring wavelength tunability in OPOSSUM.** (a) Wavemeter measurement of ν_i versus ν_p at 11 different temperatures (corresponding to the 11 different colors). The temperature is used to coarsely tune ν_i, while controlling ν_p enables fine tuning. Inset: Wavemeter measurement of ν_i versus time during a ν_p sweep. (b) Optical spectra zoomed into the idler, signal, and pump bands at each temperature (left, center, and right panels, respectively). These measurements show that output power is maintained across the tuning range.

Next, we investigate the OPOSSUM efficiency and threshold behavior. To model OPOSSUM, we simulate a pair of coupled LLEs that describe the intraresonator evolution of CW and CCW fields. We are especially interested in connections between our experimental parameters and the power generated in signal and idler waves. Intuitively, we expect the signal wave, which occupies the '+' supermode, to propagate in both CW and CCW directions; hence, we should detect some signal light at the input (reflection) port of a device, as shown in Fig. 5a. In simulations, we observe approximately 20 percent more signal power in the reflection port than the transmission port. This distribution is approximately independent of $P_{\rm in}$ and $\Delta\nu_+$. In experiments, we measure an approximately equal distribution of signal power to the two ports. The top panel of Fig. 5b shows optical spectra calibrated to estimate the on-chip power levels at the transmission (blue) and reflection (purple) ports of the OPOSSUM device characterized in Fig. 5. The presence of reflected pump and idler light is due to Fresnel reflections at the waveguide facets, but such light is still strongly suppressed relative to the transmission port (e.g, $\approx$20 dB for the idler). Ultimately, large optical losses that occur during propagation from the reflection port to the optical spectrum analyzer prevent a precise measurement of the signal power distribution. A more precise comparison can be made between the transmitted powers of the signal and idler waves, denoted $P_{\rm s}$ and $P_{\rm i}$, respectively. Specifically, we calculate $P_{\rm i}/P_{\rm s}$ versus $P_{\rm in}$ and indicate our measurements with blue data points in the bottom panel of Fig. 5b. Our measurements agree with simulation results shown by the orange dashed line. Notably, we find that $P_{\rm i}/P_{\rm s}$ does not depend on $P_{\rm in}$. Moreover, the unequal distribution of photons between signal and idler waves is unique within the Kerr microring resonator platform - previous (non-OPOSSUM) μOPO systems exhibited an equal distribution of photons ensured by the symmetry of degenerate FWM [25]. In OPOSSUM, this symmetry is broken by CW/CCW coupling. Finally, we note that signal light propagating in the CW/CCW directions can be coherently re-combined outside the resonator to increase $P_{\rm s}$.

To further characterize OPOSSUM, we measure the threshold power for parametric oscillation, $P_{\rm th}$, that is another important parameter of μOPO systems. Conveniently, we can measure $P_{\rm th}$ versus $\Delta\nu_+$ by choosing different pump modes, as shown in Fig. 5c. The $P_{\rm th}$ values predicted from our model are shown by the blue stripe, and the $P_{\rm th}$ values predicted from a crude model (consisting of a single LLE wherein we shift the signal mode frequency by J) are shown by the gray stripe. Our measurements support the validity of our model. Next, we explore the robustness of OPOSSUM with respect to variations in J. Such an investigation conveys the design tolerance, i.e., the allowable errors in device geometry that can arise from fabrication uncertainties, of OPOSSUM. Specifically, we simulate OPOSSUM and calculate the conversion efficiency, $P_{\rm i}/P_{\rm in}$, versus J for $P_{\rm in} = 10, 20,$ and 30 mW, as shown in Fig. 5d. We find that the maximum conversion efficiency is 12.5 percent for a critically-coupled resonator, which is the same result recently derived for other μOPO systems (the maximum conversion efficiency can be increased by overcoupling the resonator, at the cost of greater $P_{\rm th}$). Moreover, the range of J values that supports a given efficiency increases with $P_{\rm in}$. For instance, to realize $P_{\rm i} \geq 2$ mW with $P_{\rm in} = 20$ mW, we find $22 \leq 2J \leq 25$ GHz, where $\kappa/2\pi = 500$ MHz and $\Delta\nu_{\rm CW} = 10$ GHz. For the device characterized in Figs. 5b-c, this corresponds roughly to $11 \leq A_{\rm mod} \leq 12.5$ nm. The possibility of increasing design tolerances using, e.g., temperature tuning, requires further study.

Finally, we explore the wavelength tunability of OPOSSUM using the same device characterized in Figs. 4 and 5. Such tunability is of practical importance to nonlinear wavelength converters aiming for, e.g., specific atomic transitions. In our experiments, we sweep $\nu_{\rm p}$ by ≈ 25 GHz in 5 seconds while sustaining a μOPO, and we observe the resulting changes to $\nu_{\rm i}$ using a wavemeter ($\nu_{\rm s}$ can be inferred from $\nu_{\rm i}$ and $\nu_{\rm p}$ using Eq. 1a). An example of these data is shown in the inset to Fig. 6a. We find $\frac{d\nu_{\rm i}}{d\nu_{\rm p}} \approx 1$. To extend the wavelength access of our OPOSSUM device, we increase its temperature, T, according to $\frac{d\nu_0}{dT} \approx 4$ GHz/K and repeat the $\nu_{\rm p}$ sweep while recording $\nu_{\rm i}$. Figure 6a shows our results from repeating this measurement at 11 different temperatures (corresponding to the 11 different colors in Fig. 6), from $T \approx 295$ K to $T \approx 340$ K, chosen to access all frequencies between $367.73 \leq \nu_{\rm i} \leq 368.02$ THz. (At some temperatures, we found that $\nu_{\rm p}$ could be swept > 25 GHz while sustaining the μOPO. This is why some colors comprise more frequencies than others in Fig. 6a). At each temperature, we record the optical spectrum, as shown in Fig. 6b where we have magnified the idler, signal, and pump bands in the left, center, and right panels, respectively. Importantly, the μOPO output power is maintained across the entire tuning range. Moreover, the nearly 300 GHz of tuning reported here was limited by instabilities in our setup at the higher temperatures. Given such stability, we expect that greater tuning ranges, possibly exceeding the FSR, are attainable. Our measurements suggest that a suitable choice of N, combined with continuous tunability, gives deterministic wavelength control with high accuracy.

IV. DISCUSSION

Importantly, through the OPOSSUM mechanism we achieve 99.7 % wavelength accuracy without iterating fabrication runs (i.e., to target specific wavelengths, we identify N values based only on our finite-element simulations, with little guidance from previous measurements). Moreover, temperature tuning beyond the ≈ 50 K range we could achieve in experiments will compensate for wavelength inaccuracies. In cases where $\Delta\nu_+$ depends on T, one can leverage the relationship between $\Delta\nu_+$ and m_p. For instance, if T must be adjusted so much that a μOPO is destabilized when pumping mode m_p, then switching to $m_\mathrm{p} \pm 1$ (depending on whether T has been increased or decreased) will restore frequency matching.

In conclusion, we have shown that coherent coupling in photonic crystal resonators can facilitate FWM-based nonlinear wavelength conversion without higher-order GVD. We theoretically investigated four $\chi^{(3)}$ processes within such resonators: FWM-BS, THG, dispersive-wave enhancements in microcombs, and μOPO. In all cases we found that large efficiencies could be achieved for a specific targeted mode, establishing a basis for wavelength accuracy in Kerr-nonlinear photonics, and future optimization of the method should lead to even larger efficiencies than we report here. Moreover, we explored how the photonic crystal structure gives unprecedented control over generated wavelengths while protecting the FWM process from unwanted nonlinear couplings. To affirm simulation results, we experimentally focus on the specific case of μOPO, which is typically distinguished by a substantial sensitivity of the output wavelengths to the device geometry and pump wavelength. We generated μOPOs with signal wavenumbers defined by the photonic crystal grating period. We measured the conversion efficiencies and threshold powers for multiple devices, and our measurements agreed with simulations. Finally, we demonstrated continuous tunability of the μOPO spectrum. Importantly, we expect that coherent coupling can be implemented in resonant $\chi^{(2)}$-nonlinear systems, in addition to the $\chi^{(3)}$ systems discussed here. The devices and methods introduced here will be invaluable to future nanotechnologies that utilize application-tuned and wavelength-accurate nonlinear photonics.

V. ACKNOWLEDGEMENTS

We thank Edgar Perez and Michal Chojnacky for providing useful feedback during preparation of the manuscript. We acknowledge funding support from the DARPA LUMOS and NIST-on-a-chip programs.

VI. AUTHOR CONTRIBUTIONS

J.S. envisioned and performed the experiments and analyzed data. X.L. fabricated devices, contributed experimental ideas, and assisted with device design. G.M. assisted with device design and helped analyze data. D.W. fabricated devices, T.R. helped characterize devices, and K.S. analyzed data and consulted on experiments.

VII. COMPETING INTERESTS

NIST/UMD have filed patent applications, with J.S., K.S., and X.L. listed as inventors. The other authors declare no competing interests.

---

[1] Andrew D Ludlow, Martin M Boyd, Jun Ye, Ekkehard Peik, and Piet O Schmidt, "Optical atomic clocks," Reviews of Modern Physics **87**, 637 (2015).

[2] Tobias Bothwell, Colin J Kennedy, Alexander Aeppli, Dhruv Kedar, John M Robinson, Eric Oelker, Alexander Staron, and Jun Ye, "Resolving the gravitational redshift across a millimetre-scale atomic sample," Nature **602**, 420–424 (2022).

[3] Stephanie Wehner, David Elkouss, and Ronald Hanson, "Quantum internet: A vision for the road ahead," Science **362**, eaam9288 (2018).

[4] Ali W Elshaari, Wolfram Pernice, Kartik Srinivasan, Oliver Benson, and Val Zwiller, "Hybrid integrated quantum photonic circuits," Nature Photonics **14**, 285–298 (2020).

[5] Daryl T Spencer, Tara Drake, Travis C Briles, Jordan Stone, Laura C Sinclair, Connor Fredrick, Qing Li, Daron Westly, B Robert Ilic, Aaron Bluestone, *et al.*, "An optical-frequency synthesizer using integrated photonics," Nature **557**, 81–85 (2018).

[6] Zachary L Newman, Vincent Maurice, Tara Drake, Jordan R Stone, Travis C Briles, Daryl T Spencer, Connor Fredrick, Qing Li, Daron Westly, Bojan R Ilic, *et al.*, "Architecture for the photonic integration of an optical atomic clock," Optica **6**, 680–685 (2019).

[7] Johann Riemensberger, Anton Lukashchuk, Maxim Karpov, Wenle Weng, Erwan Lucas, Junqiu Liu, and Tobias J Kippenberg, "Massively parallel coherent laser ranging using a soliton microcomb," Nature **581**, 164–170 (2020).

[8] Alexander L Gaeta, Michal Lipson, and Tobias J Kippenberg, “Photonic-chip-based frequency combs,” nature photonics **13**, 158–169 (2019).

[9] Xiyuan Lu, Gregory Moille, Ashutosh Rao, Daron A Westly, and Kartik Srinivasan, “On-chip optical parametric oscillation into the visible: generating red, orange, yellow, and green from a near-infrared pump,” Optica **7**, 1417–1425 (2020).

[10] Noel Lito B Sayson, Toby Bi, Vincent Ng, Hoan Pham, Luke S Trainor, Harald GL Schwefel, Stéphane Coen, Miro Erkintalo, and Stuart G Murdoch, “Octave-spanning tunable parametric oscillation in crystalline kerr microresonators,” Nature Photonics **13**, 701–706 (2019).

[11] Gabriel Marty, Sylvain Combrié, Fabrice Raineri, and Alfredo De Rossi, “Photonic crystal optical parametric oscillator,” Nature Photonics **15**, 53–58 (2021).

[12] Z Vernon, N Quesada, M Liscidini, B Morrison, M Menotti, K Tan, and JE Sipe, “Scalable squeezed-light source for continuous-variable quantum sampling,” Physical Review Applied **12**, 064024 (2019).

[13] Avik Dutt, Kevin Luke, Sasikanth Manipatruni, Alexander L Gaeta, Paulo Nussenzveig, and Michal Lipson, “On-chip optical squeezing,” Physical Review Applied **3**, 044005 (2015).

[14] Michael Kues, Christian Reimer, Joseph M Lukens, William J Munro, Andrew M Weiner, David J Moss, and Roberto Morandotti, “Quantum optical microcombs,” Nature Photonics **13**, 170–179 (2019).

[15] Xiyuan Lu, Qing Li, Daron A Westly, Gregory Moille, Anshuman Singh, Vikas Anant, and Kartik Srinivasan, “Chip-integrated visible–telecom entangled photon pair source for quantum communication,” Nature physics **15**, 373–381 (2019).

[16] Qing Li, Marcelo Davanço, and Kartik Srinivasan, “Efficient and low-noise single-photon-level frequency conversion interfaces using silicon nanophotonics,” Nature Photonics **10**, 406–414 (2016).

[17] Tal Carmon and Kerry J Vahala, “Visible continuous emission from a silica microphotonic device by third-harmonic generation,” Nature Physics **3**, 430–435 (2007).

[18] Joshua B Surya, Xiang Guo, Chang-Ling Zou, and Hong X Tang, “Efficient third-harmonic generation in composite aluminum nitride/silicon nitride microrings,” Optica **5**, 103–108 (2018).

[19] Robert W Boyd, *Nonlinear optics* (Academic press, 2020).

[20] Ki Youl Yang, Katja Beha, Daniel C Cole, Xu Yi, Pascal Del'Haye, Hansuek Lee, Jiang Li, Dong Yoon Oh, Scott A Diddams, Scott B Papp, *et al.*, "Broadband dispersion-engineered microresonator on a chip," Nature Photonics **10**, 316–320 (2016).

[21] Yoshitomo Okawachi, Michael RE Lamont, Kevin Luke, Daniel O Carvalho, Mengjie Yu, Michal Lipson, and Alexander L Gaeta, "Bandwidth shaping of microresonator-based frequency combs via dispersion engineering," Optics letters **39**, 3535–3538 (2014).

[22] Xiyuan Lu, Gregory Moille, Qing Li, Daron A Westly, Anshuman Singh, Ashutosh Rao, Su-Peng Yu, Travis C Briles, Scott B Papp, and Kartik Srinivasan, "Efficient telecom-to-visible spectral translation through ultralow power nonlinear nanophotonics," Nature Photonics **13**, 593–601 (2019).

[23] Su-Peng Yu, Travis C Briles, Gregory T Moille, Xiyuan Lu, Scott A Diddams, Kartik Srinivasan, and Scott B Papp, "Tuning kerr-soliton frequency combs to atomic resonances," Physical Review Applied **11**, 044017 (2019).

[24] Travis C Briles, Jordan R Stone, Tara E Drake, Daryl T Spencer, Connor Fredrick, Qing Li, Daron Westly, BR Ilic, Kartik Srinivasan, Scott A Diddams, *et al.*, "Interlocking kerr-microresonator frequency combs for microwave to optical synthesis," Optics letters **43**, 2933–2936 (2018).

[25] Jordan R Stone, Gregory Moille, Xiyuan Lu, and Kartik Srinivasan, "Conversion efficiency in kerr-microresonator optical parametric oscillators: From three modes to many modes," Physical Review Applied **17**, 024038 (2022).

[26] Y Zhang, M Menotti, K Tan, VD Vaidya, DH Mahler, LG Helt, L Zatti, M Liscidini, B Morrison, and Z Vernon, "Squeezed light from a nanophotonic molecule," Nature communications **12**, 1–6 (2021).

[27] Yulong Tang, Zheng Gong, Xianwen Liu, and Hong X Tang, "Widely separated optical Kerr parametric oscillation in AlN microrings," Optics Letters **45**, 1124–1127 (2020).

[28] Darius Urbonas, Armandas Balčytis, Konstantinas Vaškevičius, Martynas Gabalis, and Raimondas Petruškevičius, "Air and dielectric bands photonic crystal microringresonator for refractive index sensing," Optics Letters **41**, 3655–3658 (2016).

[29] Stanley M Lo, Shuren Hu, Girija Gaur, Yiorgos Kostoulas, Sharon M Weiss, and Philippe M Fauchet, "Photonic crystal microring resonator for label-free biosensing," Optics express **25**, 7046–7054 (2017).

[30] Xiyuan Lu, Andrew McClung, and Kartik Srinivasan, "High-q slow light and its localization in a photonic crystal microring," Nature Photonics **16**, 66–71 (2022).

[31] Su-Peng Yu, Daniel C Cole, Hojoong Jung, Gregory T Moille, Kartik Srinivasan, and Scott B Papp, "Spontaneous pulse formation in edgeless photonic crystal resonators," Nature Photonics **15**, 461–467 (2021).

[32] Xiyuan Lu, Ashish Chanana, Feng Zhou, Marcelo Davanco, and Kartik Srinivasan, "Kerr optical parametric oscillation in a photonic crystal microring for accessing the infrared," Optics Letters **47**, 3331–3334 (2022).

[33] Jennifer A Black, Grant Brodnik, Haixin Liu, Su-Peng Yu, David R Carlson, Jizhao Zang, Travis C Briles, and Scott B Papp, "Optical-parametric oscillation in photonic-crystal ring resonators," Optica **9**, 1183–1189 (2022).

[34] Xiyuan Lu, Ashutosh Rao, Gregory Moille, Daron A Westly, and Kartik Srinivasan, "Universal frequency engineering tool for microcavity nonlinear optics: multiple selective mode splitting of whispering-gallery resonances," Photonics research **8**, 1676–1686 (2020).

[35] Gregory Moille, Xiyuan Lu, Jordan Stone, Daron Westly, and Kartik Srinivasan, "Arbitrary microring dispersion engineering for ultrabroad frequency combs: Photonic crystal microring design based on fourier synthesis," arXiv preprint arXiv:2210.14108 (2022).

[36] Erwan Lucas, Su-Peng Yu, Travis C Briles, David R Carlson, and Scott B Papp, "Tailoring microcombs with inverse-designed, meta-dispersion microresonators," arXiv preprint arXiv:2209.10294 (2022).

[37] Gregory Moille, Daron Westly, Ndubuisi George Orji, and Kartik Srinivasan, "Tailoring broadband kerr soliton microcombs via post-fabrication tuning of the geometric dispersion," Applied Physics Letters **119**, 121103 (2021).

[38] JiaCheng Liu, Qilin Zheng, GongYu Xia, Chao Wu, ZhiHong Zhu, and Ping Xu, "Tunable frequency matching for efficient four-wave-mixing bragg scattering in microrings," Optics Express **29**, 36038–36047 (2021).

VIII. METHODS

A. Fabrication methods

We deposit stoichiometric SiN (Si_3N_4) by low-pressure chemical vapor deposition on top of a 3 μm-thick layer of SiO_2 on a 100 mm diameter Si wafer. We fit ellipsometer measurements of the wavelength-dependent SiN refractive index and layer thicknesses to an extended Sellmeier model. The device pattern is created in positive-tone resist by electron-beam lithography and then transferred to SiN by reactive ion etching using a CF_4/CHF_3 chemistry. After cleaning the devices, we anneal them for four hours at 1100 °C in N_2. Next, we perform a liftoff of SiO_2 so that the resonator has an air top-cladding for dispersion purposes while the perimeter of the chip is SiO_2-clad for better coupling to lensed optical fibers. The facets of the chip are then polished for lensed-fiber coupling. After polishing, the chip is annealed again.

B. $\Delta\nu$ measurements

To measure $\Delta\nu$ in our devices, we use laser transmission spectroscopy to measure the resonance frequencies of TE0 resonator modes in the wavelength regions of interest, and $\Delta\nu$ is calculated according to Eq. 2. We use a tunable, CW Titanium:Sapphire (TiS) laser to perform spectroscopy. We tune the TiS laser to a TE0 resonator mode, minimize the transmission, and record the TiS frequency using a wavemeter. The TiS laser power is kept < 1 μW to avoid thermo-optic mode frequency shifts.

IX. DATA AVAILABILITY

The datasets generated during and/or analysed during the current study are available from the corresponding author on reasonable request.

X. CODE AVAILABILITY

The programs used to simulate coupled mode and Lugiato-Lefever equations are available from the corresponding author on reasonable request.

CONTENTS

I. SIMULATION METHODS

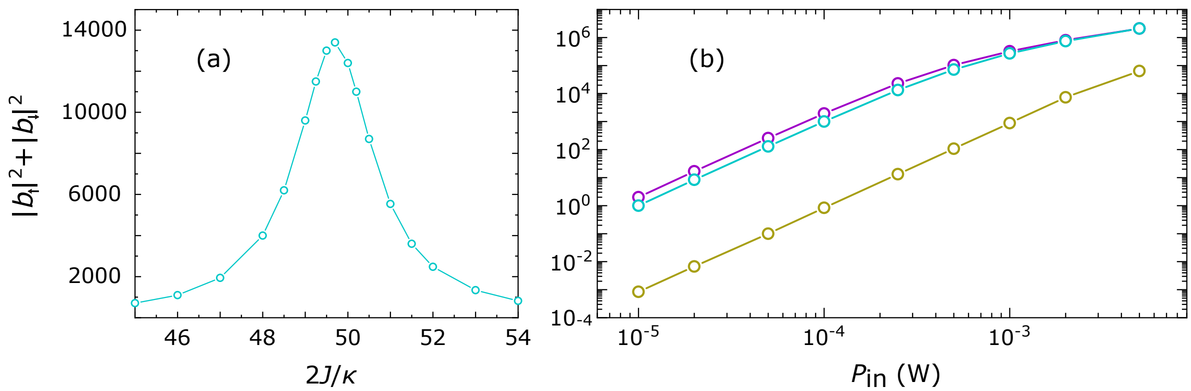

FIG. S1. **Simulation analysis of THG in Kerr photonic crystal microresonators.** (a) Third harmonic power, P_{3H}, versus normalized coupling rate, J, for $P_{\mathrm{in}} = 250\ \mu$W and $\Delta\nu = 50 \times \kappa/2$. (b) P_{3H} versus P_{in}. In these data, the pump frequency is tuned to maximize output power. The purple data correspond to $\Delta\nu \approx 0$, where $\Delta\nu$ is tuned to maximize output power. Blue and gold data correspond to $\Delta\nu = 50 \times \kappa/2$, where for blue data, J is tuned to maximize output power, and $J = 0$ for gold data. The y axes have units of photon number.

In our simulations, we assume critically-coupled resonator modes, although the equations are easy to generalize. In the case of THG, we numerically integrate a set of coupled-mode equations (CMEs) that describe the evolution of intraresonator complex field variables a, $b_\uparrow$, and $b_\downarrow$, where a denotes the pump field with angular frequency ω_{p}, and $b_{\uparrow(\downarrow)}$ denotes the generated third-harmonic field with angular frequency $3\omega_{\mathrm{p}}$ that co-propagates (counter-propagates) with the pump field. The CMEs are [1]:

$$\begin{aligned}
\frac{da}{dt} &= \sqrt{\frac{\kappa}{2\hbar\omega_{\mathrm{p}}}P_{\mathrm{in}}} - \left(\frac{\kappa}{2} - i2\pi\delta\right) a + ig_0\left(|a|^2 + 2|b_\uparrow|^2 + 2|b_\downarrow|^2\right) a - 3ig_0 a^{*2} b_\uparrow \\
\frac{db_\uparrow}{dt} &= -\left(\frac{\kappa}{2} - i2\pi(\delta + \Delta\nu/2)\right) b_\uparrow + ig_0\left(2|a|^2 + |b_\uparrow|^2 + 2|b_\downarrow|^2\right) b_\uparrow - ig_0 a^3 - iJb_\downarrow \\
\frac{db_\downarrow}{dt} &= -\left(\frac{\kappa}{2} - i2\pi(\delta + \Delta\nu/2)\right) b_\downarrow + ig_0\left(2|a|^2 + 2|b_\uparrow|^2 + |b_\downarrow|^2\right) b_\downarrow - iJb_\uparrow
\end{aligned} \tag{1}$$

where $\delta = (\omega_0 - \omega_{\mathrm{p}})/2\pi$ is the pump-resonator frequency detuning, $\Delta\nu = (\omega_b - 3\omega_{\mathrm{p}})/2\pi$ is the frequency mismatch where ω_{b} is the angular resonance frequency of the third-harmonic mode, and g_0 is the single-photon nonlinear coupling (whose frequency dependence we neglect). Note that, in Eq. 1, J has units rad/s, whereas it has units of Hz in the main text.

In Fig. S1, we characterize our THG simulations. When $\Delta\nu = 50 \times \kappa/2$, the value of J that maximizes the third harmonic power, $P_{3H} = |b_\uparrow|^2 + |b_\downarrow|^2$, is not exactly $\Delta\nu$ due to self- and cross-phase modulation. Figure S1a shows $P_{3\mathrm{H}}$ versus J for $P_{\mathrm{in}} = 250$ μW. In Fig. S1b, we present simulated values of $P_{3\mathrm{H}}$ versus P_{in}. For each data point, we tune ω_{p} to maximize $P_{3\mathrm{H}}$. The data exhibit the expected cubic dependence of P_{3H} on P_{in}; when P_{in} becomes large, the conversion saturates. Intriguingly, we observe that, below saturation, $P_{3\mathrm{H}}$ is two times larger in non-photonic-crystal resonators where $\Delta\nu \approx 0$. However, in the saturation regime, the photonic crystal resonators generate the same $P_{3\mathrm{H}}$ values as the non-photonic-crystal resonators.

To analyze FWM-BS, DWE, and μOPO in photonic crystal resonators, we simulate two coupled LLE-type equations using the split-step Fourier method. The LLE is widely used to study microcombs because it encapsulates nonlinear interactions between many resonator modes using a single equation. Our coupled LLEs describe the evolution of CW and CCW intraresonator fields, denoted as $a_\uparrow$ and $a_\downarrow$, respectively. The equations are:

$$\begin{aligned}\frac{da_{\uparrow,\downarrow}}{dt} &= \sqrt{\frac{\kappa}{2\hbar\omega_{\mathrm{p}}} P_{\mathrm{in}}} \left(1 + \sum_i F_i e^{i(\Omega_i t - \mu_i \theta)}\right) \delta_\uparrow \\ &- \left(\frac{\kappa}{2} + i\frac{\kappa}{2}\alpha\right) a_{\uparrow,\downarrow} + i\mathcal{D}(\mu)\tilde{a}_{\uparrow,\downarrow} - J(\mu)\tilde{a}_{\downarrow,\uparrow} \\ &+ i g_0 \left(|a_{\uparrow,\downarrow}|^2 + 2\int_{-\pi}^{\pi} \frac{|a_{\downarrow,\uparrow}|^2}{2\pi} d\theta\right) a_{\uparrow,\downarrow},\end{aligned} \tag{2}$$

where F_i is the amplitude, normalized to the primary pump laser amplitude, of the ith source (with frequency ω_i) injected into resonator mode μ_i (relative to the pump mode). Hence, $\Omega_i = \mathcal{D}(\mu_i) + \omega_i - \omega_\mu + \frac{\kappa}{2}\alpha$, where $\alpha = \frac{2(\omega_0 - \omega_{\mathrm{p}})}{\kappa}$ is the normalized pump-resonator detuning, $\mathcal{D}(\mu) = \omega_\mu - (\omega_0 + \mu D_1)$ is the integrated dispersion, where $D_1 = 2\pi \times \mathrm{FSR}$, $\tilde{a}_{\uparrow,\downarrow}$ indicates that operations are applied in the frequency domain, and θ is the azimuthal angle in a reference frame that moves at the group velocity (see Ref. [2] for more details). The $\delta_\uparrow$ symbol indicates the driving terms are only applied to $a_\uparrow$. There are various approximations one can make to include cross-phase modulation (XPM) in Eq. 2. Here, light travelling in each direction circulates the resonator many times in one simulation time step; therefore, we assess that XPM is suitably modeled using the averaged intraresonator intensities, $|a_{\uparrow,\downarrow}|^2$ (i.e., the final integral term in Eq. 2).

Although the frequency mismatch, $\Delta\nu$, is not explicitly included in Eq. 2, it is important to define this parameter in the case of FWM-BS, since its value dictates the required J. If the two pump modes have frequencies ν_{01} and ν_{02}, the input mode has frequency ν_{in}, and the output mode has frequency ν_{out}, then $\Delta\nu = \nu_{01} + \nu_{\mathrm{in}} - \nu_{02} - \nu_{\mathrm{out}}$.

II. A STUDY ON OPOSSUM ROBUSTNESS

In Fig. 4c of the main text, we plot our measurements of $\Delta\nu_+$ versus pump wavelength. Such a measurement indicates the robustness of μOPO generation with respect to changes in pump wavelength; specifically, minimizing the magnitude of the slope $\frac{d\Delta\nu_+}{dm_{\mathrm{p}}}$, where m_{p} is the azimuthal mode number of the pump mode, corresponds to maximizing the number of pump modes suitable to μOPO generation. Therefore, it is useful to understand the microresonator dispersion properties that primarily determine these data.

First, we write the mismatch spectrum, in the '+' basis and indexed by the azimuthal mode numbers, as

$$\Delta\nu_+ = \nu_{m_{\mathrm{s}}} + \nu_{m_{\mathrm{i}}} - 2\nu_{m_{\mathrm{p}}}, \tag{3}$$

where m_{s} is the azimuthal number of the signal mode and $m_{\mathrm{i}} = 2m_{\mathrm{p}} - m_{\mathrm{s}}$ is the azimuthal number of the idler mode. Because $m_{\mathrm{s}} = N/2$ is chosen solely by the periodic modulation of the resonator sidewall, it is independent of m_{p}. Hence,

$$\begin{aligned} \frac{d\Delta\nu_+}{dm_{\mathrm{p}}} &= \frac{d}{dm_{\mathrm{p}}}(\nu_{m_{\mathrm{s}}} + \nu_{m_{\mathrm{i}}} - 2\nu_{m_{\mathrm{p}}}) \\ &\approx 0 + 2FSR_{m_{\mathrm{i}}} - 2FSR_{m_{\mathrm{p}}}, \end{aligned} \tag{4}$$

where FSR_m is the free spectral range around the mode with azimuthal number m. Clearly, to minimize the magnitude of $\frac{d\Delta\nu_+}{dm_{\mathrm{p}}}$, the pump and idler spectral regions should exhibit nearly equal FSR values. For the devices studied in the main text, which show sufficient robustness for the μOPO signal frequency to remain fixed while the pump frequency changes by ≈ 4 THz, the FSR mismatch between idler and pump is ≈ 300 MHz. We note that no special care was taken to design a device exhibiting a smaller mismatch, but we anticipate that future designs could be developed in which a much smaller mismatch can be obtained while still maintaining frequency matching for the overall μOPO process. This is a consequence of the flexibility afforded by the OPOSSUM scheme, where in this case, the underlying dispersion could be chosen to optimize robustness (i.e., FSR mismatch between the pump and idler bands) and the photonic crystal splitting chosen to ensure that such a geometry satisfies frequency matching.

Finally, we note that conventional μOPO devices rely on higher-order GVD for frequency matching; correspondingly, the idler spectral region typically exhibits strong anomalous dispersion and a FSR substantially (many linewidths) smaller than the pump region. In general, these devices lack the ability to simultaneously minimize the FSR mismatch between idler and pump bands while still achieving frequency matching for the μOPO process.

III. COMPARING PHOTONIC-CRYSTAL FREQUENCY MATCHING SCHEMES

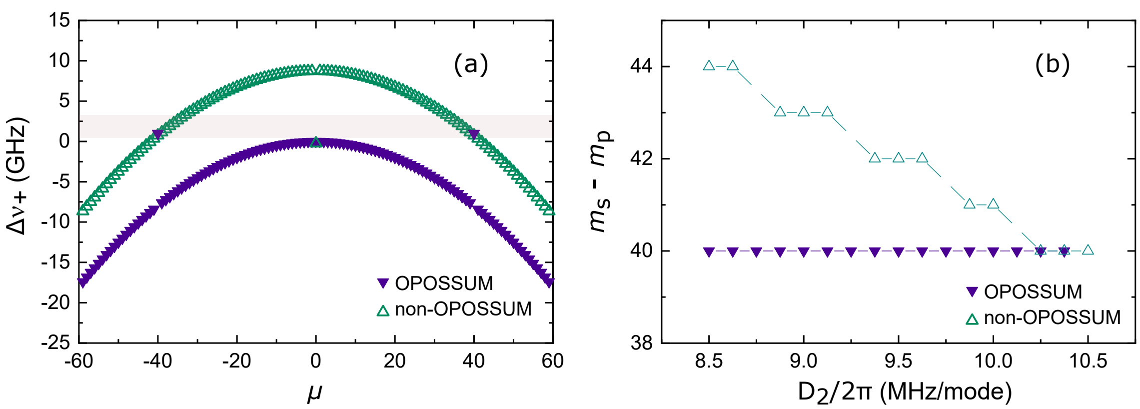

FIG. S2. **Theoretical comparison between OPOSSUM and frequency matching by pump-mode photonic crystal splitting.** (a) Frequency mismatch, $\Delta\nu_+(\mu)$, versus μ for an OPOSSUM device (filled-in triangles) and a device in which the photonic-crystal splitting is applied to the pump mode (hollow triangles). For the OPOSSUM device, J = 17.5 GHz and the splitting targets mode $\mu = 41$. For the non-OPOSSUM device, J = 8.75 GHz and the splitting targets mode $\mu = 0$. In both devices, $D_2/2\pi$ = 10 MHz/mode. The pale strip marks the range of $\Delta\nu_+$ values that support μOPO. (b) μOPO separation, $m_\mathrm{s} - m_\mathrm{p}$, versus $D_2/2\pi$ for devices similar to those from (a). For the OPOSSUM (non-OPOSSUM) device, P_in = 15(30) mW. In both devices, the (critically-coupled) modal linewidth is $\kappa/2\pi$ = 500 MHz.

Another way to realize frequency matching in μOPO devices is to apply a photonic-crystal mode splitting to the pump mode instead of the signal or idler modes (we refer to these devices as being "non-OPOSSUM"). This scheme has been studied in prior works [3, 4], and in this section we show that, while both methods can facilitate FWM in microresonators with normal GVD, OPOSSUM uniquely enables wavelength accuracy, tunability, and robustness. Figure S2a depicts $\Delta\nu_+$ spectra for one OPOSSUM and one non-OPOSSUM device with the same underlying normal GVD. In both cases, OPO between widely separated modes can be realized. However, the key difference is that OPOSSUM isolates one mode pair for oscillation, while in the non-OPOSSUM device multiple mode pairs exhibit $\Delta\nu_+$ values suitable for μOPO. These modes compete for gain and reduce the accuracy with which specific wavelengths may be targeted. To demonstrate this point, in Fig. S2 we present the resulting μOPO separation, $m_\mathrm{s} - m_\mathrm{p}$ that we extract from LLE simulations, versus the underlying microresonator dispersion, $D_2/2\pi$. We choose $D_2/2\pi$ as the axis variable because this parameter is sensitive to both the microresonator geometry and, in practice, temperature. Hence, such a study indicates both the robustness with which a specific signal mode can be targeted and the continuous tunability of the resulting μOPO wavelengths. In the OPOSSUM device, $m_\mathrm{s} - m_\mathrm{p}$ is independent of the dispersion as it is defined only by the photonic crystal grating period. In the non-OPOSSUM device, we observe mode switching [5], which shows how the non-OPOSSUM μOPO is less robust and tunable than its OPOSSUM counterpart.

[1] Noel Lito B Sayson, Toby Bi, Vincent Ng, Hoan Pham, Luke S Trainor, Harald GL Schwefel, Stéphane Coen, Miro Erkintalo, and Stuart G Murdoch, "Octave-spanning tunable parametric oscillation in crystalline kerr microresonators," Nature Photonics **13**, 701–706 (2019).

[2] Hossein Taheri, Andrey B Matsko, and Lute Maleki, "Optical lattice trap for kerr solitons," The European Physical Journal D **71**, 1–13 (2017).

[3] Jennifer A Black, Grant Brodnik, Haixin Liu, Su-Peng Yu, David R Carlson, Jizhao Zang, Travis C Briles, and Scott B Papp, "Optical-parametric oscillation in photonic-crystal ring resonators," Optica **9**, 1183–1189 (2022).

[4] Xiyuan Lu, Ashish Chanana, Feng Zhou, Marcelo Davanco, and Kartik Srinivasan, "Kerr optical parametric oscillation in a photonic crystal microring for accessing the infrared," Optics Letters **47**, 3331–3334 (2022).

[5] Jordan R Stone, Gregory Moille, Xiyuan Lu, and Kartik Srinivasan, "Conversion efficiency in

kerr-microresonator optical parametric oscillators: From three modes to many modes," Physical Review Applied **17**, 024038 (2022).